Structural Defects in Donor-Acceptor Blends: Influence on the Performance of Organic Solar Cells

Natalia Sergeeva,* Sascha Ullbrich, Andreas Hofacker, Christian Koerner, and Karl Leo†

Dresden Integrated Center for Applied Physics and Photonic Materials, Technische Universitaet Dresden, D-01062 Dresden, Germany

(Received 14 September 2017; revised manuscript received 12 December 2017; published 28 February 2018)

Defects play an important role in the performance of organic solar cells. The investigation of trap states and their origin can provide ways to further improve their performance. Here, we investigate defects in a system composed of the small-molecule oligothiophene derivative DCV5T-Me blended with C_{60}, which shows power conversion efficiencies above 8% when used in a solar cell. From a reconstruction of the density of trap states by impedance spectroscopy, we obtain a Gaussian distribution of trap states with $E_t = 470$ meV below the electron transport level, $N_t = 8 \times 10^{14}$ cm^{-3}, and $\sigma_t = 41$ meV. From V_{oc} vs illumination intensity and open-circuit corrected charge carrier extraction measurements, we find that these defects lead to trap-assisted recombination. Moreover, drift-diffusion simulations show that the trap states decrease the fill factor by 10%. By conducting degradation measurements and varying the blend ratio, we find that the observed trap states are structural defects in the C_{60} phase due to the distortion of the natural morphology induced by the mixing.

DOI: 10.1103/PhysRevApplied.9.024039

I. INTRODUCTION

Organic photovoltaics (OPV) is a promising technology for renewable energy production. OPV is potentially cheaper in production than inorganic photovoltaics and can be used on different surfaces due to the possibility of processing on flexible substrates.

Organic photovoltaics can be based on polymers or on small molecules. Small molecules can be both vacuum and solution processed, offer better control over material purity through sublimation, and do not suffer from polydispersity as polymers. Power conversion efficiencies (PCEs) above 11% have been achieved for both types of organic solar cells [1–7], with a maximum efficiency of 13.2% reported for small-molecule multijunction solar cells (SCs) by Heliatek and 13.1% for polymer-based SCs [4].

Although these PCE values are rather promising from an application point of view, the efficiency is still limited by the charge-carrier transport in the organic material. For example, it is known that intragap states (traps) can limit charge-carrier transport [8]. Organic materials are particularly prone to the formation of trap states due to their disordered nature caused by the weak van der Waals attraction between molecules, disturbance of the crystalline thin-film growth by simultaneous deposition of donor and acceptor, and low material purity. Traps increase energetic disorder and induce trap-assisted recombination, which in turn leads to a decrease in the charge-carrier densities, the open-circuit voltage, and the amount of charge carriers extracted at the electrodes as a photocurrent [9,10]. Particularly, they modify the internal electric field and decrease the charge carrier mobility by temporarily trapping charge carriers, thus hampering the photocurrent [11,12]. There are several reports in the literature about the identification of energetic distributions of trap states and their origin in organic materials [13–18]. However, no investigation of trap states has been done for oligothiophenes in spite of their excellent performance in organic solar cells. Here, we focus on dicyanovinyl end-capped oligothiophene DCV5T-Me (Fig. 1) blended with C_{60}, which showed high efficiencies in vacuum-processed small-molecule organic solar cells with a PCE of the best single-junction cell of 8.3% and a fill factor (FF) of 65.8% [19–21].

We determine the energetic distribution of defects in DCV5T-Me:C_{60} blends, define their type (hole or electron), and investigate the origin of trap states by performing impedance spectroscopy (IS) measurements. By obtaining the ideality factor at different light intensities, we find that the observed trap states lead to trap-assisted recombination.

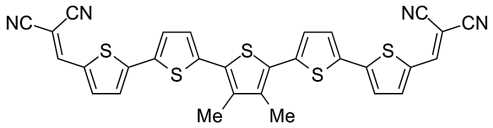

FIG. 1. Chemical structure of DCV5T-Me ([2,2′-([3″,4″-dimethyl-(2,2′:5′,2″:5″,2‴:5‴,2⁗-quinquethiophene)-5,5⁗-diyl]bis(methanylylidene))dimalononitrile]).

*natalia.sergeeva@iapp.de
†leo@iapp.de

 © 2018 American Physical Society

Finally, drift-diffusion simulations of current-voltage (I-V) curves show that the observed trap states are responsible for a reduction of the FF by 10%.

II. EXPERIMENTAL PROCEDURES

A. Sample preparation

All samples are processed by thermal evaporation under ultrahigh vacuum with a base pressure $< 10^{-8}$ mbar (Kurt J. Lesker Co., England). The samples are evaporated on indium tin oxide (ITO) (90 nm with 26 Ω/sq) coated glass substrate, working as an anode. Before processing, the wafer is heated at 90 °C for 15 min. The substrate is heated at 80 °C during the deposition of DCV5T-Me containing layers. All measured devices with a DCV5T-Me:C_{60} blend have the mixing ratio of 2:1 by volume that has been determined to be optimal for the solar cell. Additionally, in the blend variation measurements, blend ratios of 1:1 and 1:2 are used. As the top electrode, a 100-nm-thick layer of Al is used. The processing-relevant information for the materials used is summarized in Table I. All samples are encapsulated with epoxy glue and glass in a nitrogen atmosphere after deposition. The active area of all devices is 6.44 mm^2, as defined by the intersection of the ITO and Al contacts.

B. Impedance spectroscopy

Impedance spectroscopy measurements are performed with an Autolab PGSTAT302N. Capacitance frequency spectra are measured at 0 V bias voltage and 20 mV amplitude of the applied sinusoidal voltage. The measurement frequency is varied from 1 to 10^6 Hz. For measuring C-f spectra at different temperatures, we use a Peltier element that allows for temperature variation between −50 °C and 50 °C. To prevent the formation of ice at $T < 0$ °C, the sample is placed in an evacuated chamber (air pressure of 1 mbar).

For the reconstruction of the trap DOS from the C-f spectra, frequencies above 10^5 Hz are excluded from the analysis to avoid artifacts from series resistance. Since the derivative $dC/d\omega$ is used, even moderate deviations in smoothness of the C-f curve can lead to a big scattering in the reconstructed DOS. For this reason, the most scattered points in the DOS and frequencies $\omega < 10^2$ Hz are excluded from the evaluation.

TABLE I. Overview of the materials used.

Material	Evaporation rate, Å/s	Density, g/cm^3	Supplier
DCV5T-Me	0.1	1.3	Synthon Chemicals
C_{60}	0.1	1.63	CreaPhys
Al	2	2.73	Kurt J. Lesker
BPAPF	0.4	1.2	Lumtec
NDP9	0.6	1.2	Novaled
W2(hpp)4	0.3	1.63	Novaled

C. OTRACE measurements

Open-circuit corrected charge carrier extraction (OTRACE) measurements are conducted in two steps as described by Baumann *et al.* [22]. First, the sample is connected to a 1-MΩ resistor of an oscilloscope (Tektronix DPO7354C). Upon excitation with a white light-emitting diode [(LED), LUXEON K2], powered by a 100-ms-long, square-shaped pulse (Agilent 33600A), the voltage transient is recorded. A linearly increasing voltage pulse with an amplitude of 2.5 V and a duration of 60 μs is added to the already recorded $V(t)$ function after varied delay times (100 ns to 30 ms). In the second step, the modified $V(t)$ signal is applied to the sample while illuminating with the same pulsed LED as in step 1. Up to the delay time, the $V(t)$ just compensates for the field created by the generated charge carriers and keeps them in the device. The characteristic current response is recorded with the same oscilloscope and allows us to calculate the carrier density [23]. The voltages at which carrier densities are extracted are $V(\Delta t + t_{\max})$, where $t_{\max}$ is the time corresponding to the maximum of the extraction curve.

D. V_{oc} vs illumination intensity

For V_{oc} vs illumination-intensity measurements, a sun simulator (16S-003-300-AM1.5 by Solar Light Co., Glenside, Pennsylvania) is used. The intensity is changed, using neutral-density filters and changing the distance of the light source to the sample. The open-circuit voltage is recorded by a Keithley SMU 2400. Light intensities are calibrated with a reference diode (Hamamatsu S1337-33BQ) and mismatch corrected. From the slope in the intensity-voltage plot, the ideality factor is calculated [24].

E. Degradation

For the air degradation measurements, we remove the encapsulation of the device and store it in an ambient atmosphere in the dark. The sample is aged in several steps. Between the aging steps, the sample is placed in different atmospheres: 1 mbar air, a N_2 glove box with O_2 and H_2O concentrations below 0.1 ppm, and He, which does not influence the IS measurement (see the Supplemental Material [25]).

For the oxygen degradation experiment, the devices are stored at 2 bar oxygen pressure in the dark. Before being inflated with oxygen, the degradation chamber is heated at 120 °C in a 1-mbar vacuum to remove water traces. During the measurement, the device is kept in a chamber with 1 mbar air pressure. Between the measurement and the degradation, the sample is stored in a N_2 glove box with O_2 and H_2O concentrations below 0.1 ppm.

III. SIMULATION

For the drift-diffusion simulations of I-V curves of the solar cells, we divide the device into N grid points and

TABLE II. Overview of parameters used in the simulation of I-V curves.

Parameter	Value used in simulations	Measured value	Unit
Thickness	40	40	nm
Band gap	1.75	1.75[a]	eV
Effective DOS	1×10^{21}		cm^{-3}
Permittivity	5	4.4	
Electron mobility	1.0×10^{-3}[b]	6.6×10^{-3}[c]	$cm^2/(V\,s)$
Hole mobility	1.0×10^{-3}[b]	0.7×10^{-4}[d]	$cm^2/(V\,s)$
Temperature	300		K
ν_0	5×10^{11}	5×10^{11}	s^{-1}

[a]The value for the band gap is obtained from the difference between the onset of the DCV5T-Me HOMO [26] and the onset of the C_{60} LUMO [27].
[b]μ_0
[c]Electron mobility in C_{60}[28].
[d]Hole mobility in DCV5T-Me. The mobility is measured by J. Jankowski and C. Körner in-house in an organic field-effect transistor (OFET) geometry.

calculate charge-carrier densities, mobilities, recombination rates, and electric fields iteratively for each point. Mobility is calculated in the form $\mu_{\text{eff}} = \mu_0 \times n_{\text{free}}/n_{\text{total}}$, where n_{free} is the density of free charge carriers in the presence of trap states and n_{total} is the free-charge-carrier density in the absence of trap states. n_{free} and n_{total} are obtained using Boltzmann statistics. Hence, for holes, we have $n^h_{\text{free}} = n^h_{\text{total}}$ and $\mu^h_{\text{eff}} = \mu^h_0$, as we assume no hole trap states. We use the same constant mobility for free holes and electrons $\mu^e_0 = \mu^h_0 = 10^{-3}\ \text{cm}^2/(\text{V s})$. Table II gives an overview of the parameters used in simulations and the measured parameters.

IV. THEORY

We use impedance spectroscopy for the investigation of trap states. The method is based on applying an electrical signal to the device and measuring its response. We apply a small sinusoidal voltage perturbation $V = V_0 \sin(\omega t)$ at different frequencies and measure the current response $I = I_0 \sin(\omega t + \phi)$. The phase shift between the applied and measured signals ϕ and the current amplitude carry information about the electrical processes in the device.

The imaginary part of the admittance Y is proportional to the capacitance C of the device: $Y(\omega) = G(\omega) + i\omega C(\omega)$, where $G(\omega)$ is the conductance. The capacitance of a solar cell can be represented as a sum of the frequency-independent capacitance of the depletion region C_{depl} and the frequency-dependent capacitance of trap states C_t, which are populated and depopulated by the ac signal: $C(\omega) = C_{\text{depl}} + C_t(\omega)$. A given trap level can respond to the applied signal if the signal frequency is below a certain frequency,

$$\omega_t = 2\nu_0 \exp(-E_t/kT), \tag{1}$$

where E_t is the trap energy with respect to the transport level [29,30] and ν_0 is the attempt-to-escape frequency. The deeper the trap, the longer it takes to populate and depopulate it, and the lower the frequency at which it contributes to the capacitance. In the case of one discrete trap level, a steplike C-f spectrum results, with an inflection frequency that equals the trap frequency ω_t. In the case of a trap distribution, the C-f spectrum gradually increases towards lower frequencies as the amount of trap states that follow the signal increases. For a Gaussian distribution of trap states with a density of states

$$g_G(E) = \frac{N_{t,G}}{\sqrt{2\pi\sigma^2}} \exp\left(\frac{-(E - E_{t,G})^2}{2\sigma^2}\right), \tag{2}$$

the C-f spectrum shows a smeared-out (depending on the width of the Gaussian distribution), steplike behavior. In this case, the inflection frequency corresponds to the energy of the Gaussian peak: $\omega_{\text{inflection}} = 2\nu_0 \exp(-E_{t,G}/kT)$.

The trap contribution to the capacitance is calculated using a statistical Boltzmann approach as in Ref. [31]:

$$C^*_t(\omega) = \frac{q^2}{kT} \int_{E_v}^{E_c} \frac{f(E)[1 - f(E)]}{1 + i\omega/\omega_t} g(E) dE, \tag{3}$$

where C^*_t is the complex trap capacitance and $g(E)$ is a generic trap distribution. The calculation of the trap capacitance therefore requires the knowledge of the exact trap distribution as well as the energy diagram of the device.

The applied small voltage perturbations change the occupation of trap states near the Fermi level E_F. Hence, trap states crossing E_F give a maximum contribution to the capacitance, while trap states that do not cross E_F give an (exponentially) smaller contribution to the capacitance. This fact limits the resolution of trap energies to only those states that cross the Fermi level. Using first-principle rate equations, neglecting the contribution to the junction capacitance from the trap states that do not cross E_F and restricting the integration in space to the depletion region, Walter *et al.* analytically derived a formula that relates the number of trap states at E_t to the derivative of the C-f spectra [14,17,32]:

$$N_t(E_t) = -\frac{V_{\text{bi}}}{qW} \frac{\omega}{kT} \frac{dC}{d\omega}, \tag{4}$$

where V_{bi} is the built-in voltage and W is the depletion width. The trap density $N_t(E)$ is assumed to be constant within $\pm 2kT$, leading to a broadening of the reconstructed DOS for narrower trap distributions.

V. RESULTS AND DISCUSSION

A. Recombination

In this section, we investigate recombination dynamics in complete solar cells based on DCV5T-Me:C_{60} blends.

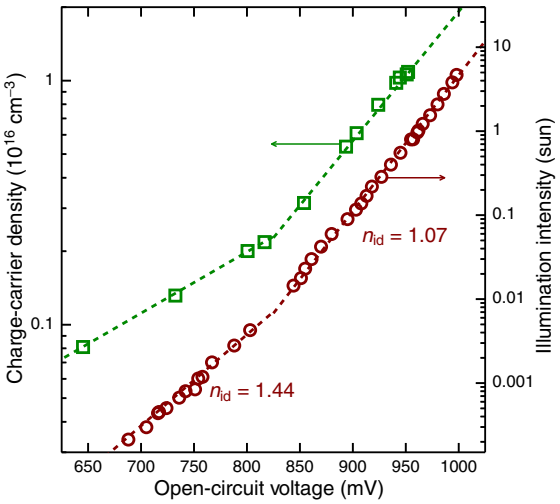

FIG. 2. Ideality factor (red) and charge-carrier density (green) measurements. The red plot has a slope of 63 mV/dec corresponding to $n_{id} = 1.07$ at light intensities above 0.01 sun and 84 mV/dec corresponding to $n_{id} = 1.44$ at intensities lower than 0.01 sun. The measurements are performed on complete solar cells ITO/C_{60}:W2(hpp)4, 4wt%,5nm/C_{60},15nm/DCV5T-Me:C_{60},2:1,100nm/BPAPF, 5nm/BPAPF:NDP9, 10wt%,45nm/Al,100nm 4 wt%, 5 nm/C_{60}, 15 nm/DCV5T-Me:C_{60}, 2:1, 100 nm/BPAPF, 5 nm/BPAPF:NDP9, 10 wt%, 45 nm/Al, 100 nm.

Therefore, we perform V_{oc} vs illumination-intensity measurements [24,33] to determine the ideality factor n_{id} and the OTRACE measurements [22,23] to find the charge-carrier concentration at different light intensities (Fig. 2). We observe two different regimes. At high light intensities above 0.01 sun, the ideality factor is close to 1, indicating bimolecular recombination. At lower light intensities and charge-carrier densities, we find an ideality factor of 1.44 that points to trap-assisted recombination.

We attribute the change in recombination mechanism to the presence of traps. In the following, we investigate those trap states in more detail using impedance spectroscopy.

B. Trap polarity

For investigation of trap states with IS, we use a simplified layer stack to avoid the influence of additional layers on the capacitance. In this section, we compare the amount of hole and electron trap states and their contribution to the capacitance. For this purpose, we use two types of stacks: ITO/DCV5T-Me:C_{60}/Al [Fig. 3(a)] and ITO/DCV5T-Me:C_{60}/BPAPF:NDP9, 10wt%/NDP9/Al, referred to as *mim* and *mip* devices, respectively. Both stacks show gradually increasing capacitance [Fig. 3(b)] towards lower frequencies, indicating the presence of trap states. A similar behavior can be caused by unintentional doping, leading to the formation of a charge depletion zone smaller than the device thickness and charge-carrier freeze-out at high frequencies [34]. To distinguish between these two effects, we perform a C-f analysis of the devices with different blend thicknesses (see the Supplemental Material [25]). The C-f spectra shift parallel to each other. This behavior indicates that the devices are completely depleted and the steplike behavior of the C-f spectra is caused by trap states and not by a transition from the geometrical to the depletion capacitance, as the latter would stay constant for all thicknesses. From the value of the geometrical capacitance, we obtain the relative permittivity of the blend of 4.4.

The *mim* device exhibits a larger trap capacitance response than the *mip* device, indicating a higher amount of trap states in the measured frequency range. In order to estimate the ratio of trap states in *mim* and *mip* devices, we assume a constant density of states. In this case, $C_t \sim \sqrt{g_t}$ [35–37], and the density of the trap states crossed by the Fermi level in the *mim* device exceeds the one in the *mip* device by a factor of 16.

The difference in C-f spectra for the two samples is caused by the different contacts allowing access to different trap energies. In the *mim* devices, only trap states with energies between the work functions of ITO (4.5 eV [38,39]) and Al (4.2 eV [40]) contribute to the C-f signal, as only these trap levels are crossed by the Fermi level

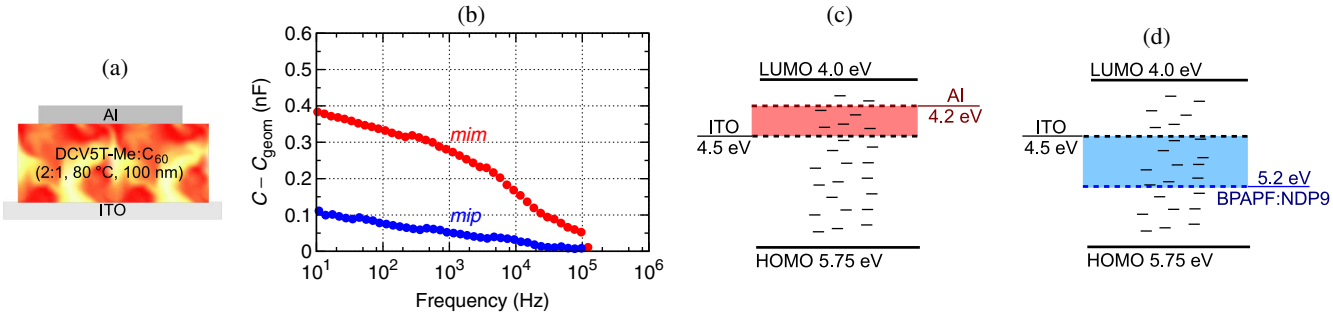

FIG. 3. (a) Device stack of ITO/DCV5T-Me:C_{60}, 100 nm/Al. (b) C-f spectra for ITO/DCV5T-Me:C_{60}, 100 nm/Al (*mim*) and ITO/DCV5T-Me:C_{60}, 130 nm/BPAPF:NDP9, 10 wt%, 45 nm/NDP9, 2 nm/Al (*mip*) devices. (c) Energy diagram of the *mim* device. We use an effective gap of DCV5T-Me:C_{60}, where holes are carried in the HOMO of DCV5T-Me and electrons are carried in the LUMO of C_{60}. (d) Energy diagram of the *mip* device. The energy diagrams are not drawn to scale.

[see Fig. 3(c)]. Hence, only electron trap states can contribute to the *C-f* spectra in *mim* devices. In *mip* devices, trap states with energies between the work function of ITO and the Fermi level of BPAPF:NDP9, 10 wt % (5.2 eV [41]) contribute to the *C-f* spectra [see Fig. 3(d)]. Trap states with energies above the work function of ITO and below the work function of BPAPF:NDP9 can only give a minor contribution to the *C-f* spectra, as they do not cross the Fermi level.

Assuming the transport energy to be at the onset of C_{60} LUMO [27] (DCV5T-Me HOMO [26]), we estimate that electron trap states with energies $E_t < 200$ meV and hole trap states with energies $E_t < 550$ meV are not accessible in these measurements (see the energy diagram in Fig. 3). These numbers are lower estimates. The transport level can be lower (higher) than the LUMO (HOMO) onset [30,42], making shallower trap states accessible.

In the following, we focus on the electron trap states (the *mim* device) due to the low signal in the *mip* device.

C. Trap DOS

We focus on electron traps [*mim* device, Fig. 3(a)] and apply the method introduced by Walter *et al.* [32] to obtain the trap DOS. First, we measure the *C-f* spectra at different temperatures [Fig. 4(a)]. As the temperature decreases, the transition from geometrical to trap capacitance shifts to lower frequencies. This shift is related to the temperature dependence of the trap response frequency $\omega_t = 2\nu_0 \exp(-E_t/kT)$. Next, we convert each *C-f* curve into the DOS [Fig. 4(b)]. We transform the frequency axis into energy using Eq. (1) and obtain the trap density using Eq. (4). We use $V_{\mathrm{bi}} = 0.3$ V defined by the difference between work functions of ITO and Al as measured by UPS. The uncertainty in V_{bi} (of 0.1 V) translates to an uncertainty in the trap density without changing the energetic distribution. For the depletion width, we use $W = 100$ nm, as the whole layer is depleted as discussed in Sec. V B.

The choice of the correct ν_0 value is essential, as it shifts the DOS along the energy axis. Assuming that DOS and ν_0 do not change in the temperature range used, the correct attempt-to-escape frequency is found when all single measurements overlap in one distribution. Hence, we obtain $\nu_0 = 5 \times 10^{11}$ s^{-1}. This value is in good agreement with the previous trap DOS reconstruction in organic small-molecule blend layers composed of ZnPc:C_{60} [14]. The resulting defect distribution has a Gaussian shape with $E_t = 470$ meV, $N_t = 8 \times 10^{14}$ cm^{-3}, and $\sigma_t = 41$ meV [Fig. 4(b)].

By applying Eq. (4), one assumes that the capacitive response of charge carriers does not depend on frequency. This assumption can be violated in organic materials due to low mobilities, leading to an overestimation of the trap depth and a wrong attempt-to-escape frequency [34]. The electron mobility in our devices is 6.6×10^{-3} cm^2/(V s) [28], which is higher than the limit mobility of 10^{-4} cm^2/(V s) [34]. Hence, we conclude that the obtained trap DOS is not affected.

D. Influence of trap states on SC parameters

Although we use a simplified device for IS measurements, the trap density of 8×10^{14} cm^{-3} (Fig. 4) that we observe in IS matches the charge-carrier density of 2×10^{15} cm^{-3}, at which we observe the change of recombination regime (Fig. 2). At high light intensities and charge-carrier densities above 2×10^{15} cm^{-3}, the charge-carrier density exceeds the amount of deep trap states $N_t = 8 \times 10^{14}$ cm^{-3} and bimolecular recombination dominates.

In order to test the influence of trap states on the SC performance, we perform one-dimensional drift-diffusion simulations for a solar cell with a single electron trap level in the active layer. We use an effective energy diagram of

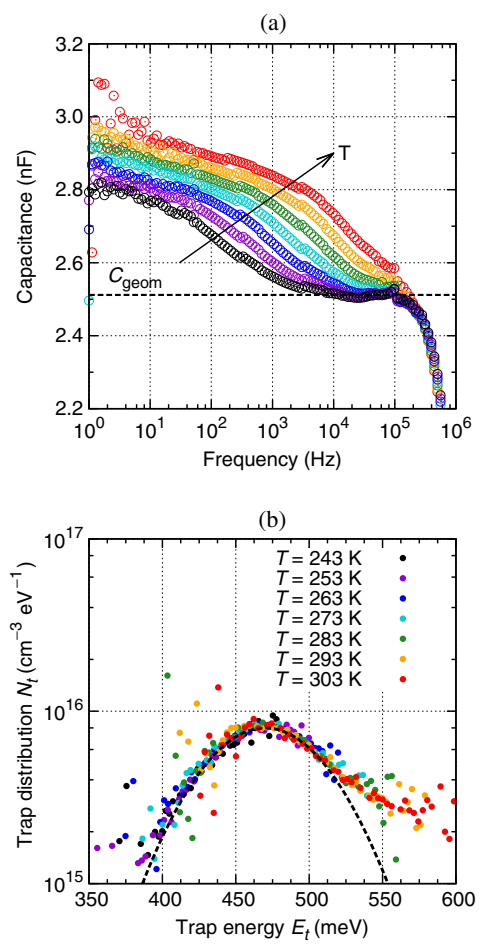

FIG. 4. (a) *C-f* spectra for the ITO/DCV5T-Me:C_{60}, 100 nm/Al device, measured at temperatures ranging from 243 to 303 K, with steps of 10 K. (b) Trap DOS reconstructed according to the approach described by Walter *et al.* [32] from the *C-f* spectra depicted in (b) using $\nu_0 = 5 \times 10^{11}$ s^{-1}. The peak is fitted with a Gaussian distribution (the black dashed line) with $E_t = 470$ meV, $N_t = 8 \times 10^{14}$ cm^{-3}, and $\sigma_t = 41$ meV.

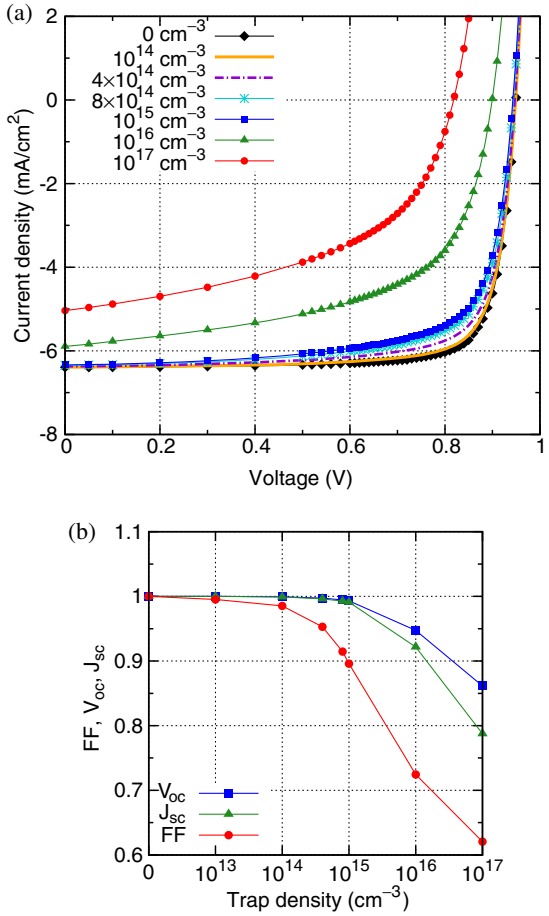

FIG. 5. (a) Simulated *I-V* curves for solar cells with a single electron trap level at 470 meV. Simulations are performed for a charge-carrier generation rate of 10^{22} cm^{-3} s^{-1} which is in the range of 1 sun. Different colors represent different densities of trap states in the device. (b) The absolute values for the fingerprints are summarized in the table in the Supplemental Material [25].

the DCV5T-Me:C_{60} blend, with electrons being transported in the C_{60} LUMO at 4.0 eV and holes being transported in the DCV5T-Me HOMO at 5.75 eV. No injection or extraction barriers are assumed, which should be a good approximation for the complete solar cell where the use of doped layers guarantees Ohmic contacts. The trap is located at 470 meV below the electron transport level, and the trap density is varied from 0 to 10^{17} cm^{-3}. We assume the transport level to be at the LUMO energy of 4.0 eV. The charge-carrier generation is taken to be 10^{22} cm^{-3} s^{-1}, corresponding to approximately 1 sun. As a recombination model, we use bimolecular recombination because the influence of trap-assisted recombination is negligible at 1 sun (Fig. 2).

The simulated *I-V* curves and the corresponding *I-V* parameters are shown in Fig. 5. The main effect of the trap states is a reduction of the FF. The defects change the number of free charge carriers, leading to a reduced mobility and, thus, a lower power conversion efficiency. For the electron trap concentration of 8×10^{14} cm^{-3} found in IS (Fig. 4), the relative reduction of the FF amounts to about 10%.

It is therefore interesting to clarify the origin of these trap states. Possible causes may be impurities in the raw materials, external impurities (e.g., ingress of air or moisture into the sample), or structural defects. Therefore, we perform degradation measurements and measure trap states in blends with varying mixing ratios.

E. Air and oxygen trap states

We distinguish between diffusion of air into the device and other types of impurities. To identify the influence of degradation, we investigate defects in decapsulated *mim* devices and compare them with the encapsulated device.

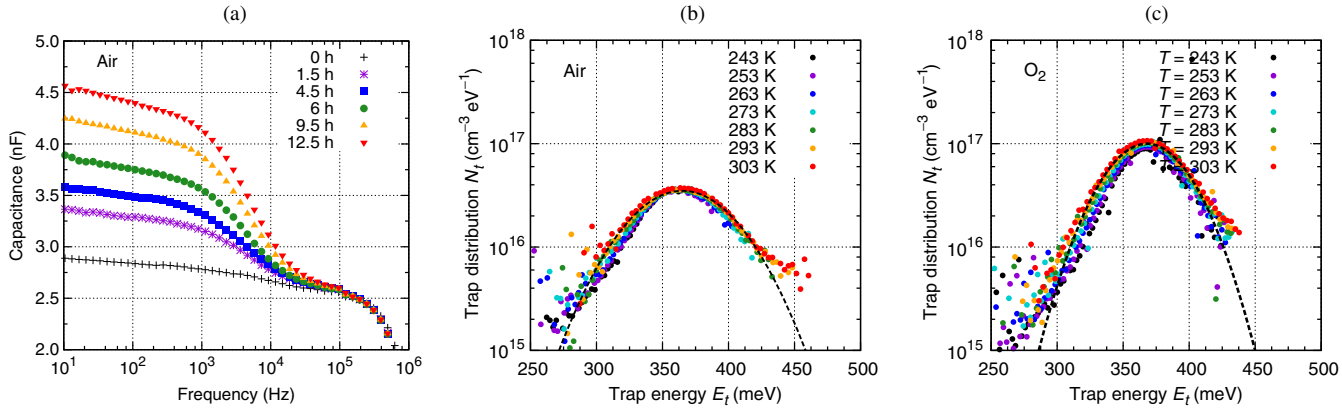

FIG. 6. (a) *C-f* spectra for an ITO/DCV5T-Me:C_{60}, 100 nm/Al device after air exposure for up to 12.5 h. (b) Trap DOS obtained for the device exposed to air. The DOS is reconstructed from the respective *C-f* curves measured at temperatures from 243 to 303 K using $\nu_0 = 2.8 \times 10^9$ s^{-1}. The black dashed line is a Gaussian fit for the peak using $E_t = 365$ meV. (c) Trap DOS obtained for an ITO/DCV5T-Me:C_{60}, 100 nm/Al device stored in oxygen. The DOS is reconstructed using $\nu_0 = 1.5 \times 10^9$ s^{-1} and is fitted with a Gaussian distribution (the black dashed line) using $E_t = 368$ meV. The trap depth compares to the air-aged devices.

We store decapsulated devices in air and an oxygen atmosphere. Degraded devices show an increase of the trap capacitance with time [Fig. 6(a)], indicating an increasing number of trap states. The trap DOS in the device kept in air is shown in Fig. 6(b). We fit a Gaussian distribution to the data and obtain $E_t = 365$ meV ($\nu_0 = 2.8 \times 10^9$ s^{-1}). Oxygen produces trap states with the same trap depth as observed in the air-aged devices [Fig. 6(c)]. We therefore conclude that the trap level observed in the air-degraded device is formed by oxygen.

Assuming the transport level to be the same in degraded and encapsulated devices (as the amount of trap states is much smaller than DOS), with $E_t = 365$ meV, the defects formed by degradation are more shallow in comparison to the traps found in previous experiments ($E_t = 470$ meV). This means that the trap state at 470 meV found in the encapsulated device is not caused by oxygen or water uptake during or after the processing but is an intrinsic nature of the blend, which will be discussed in the following.

F. Structural defects

We further consider structural defects as another possible origin for the deep trap states found in the DCV5T-Me:C_{60} blend layer. For this purpose, we further investigate samples with a pure DCV5T-Me layer and blend layers with varied mixing ratios for the presence of trap states. Although electrons are most probably transported on the acceptor phase, in the following discussion, we include the possibility of electrons to be trapped in the donor phase, especially due to the fact that the LUMO energies of DCV5T-Me and C_{60} are close to each other (less than 300 meV [20,27]).

Neat DCV5T-Me samples show only a minor increase in capacitance (see the Supplemental Material [25]), much smaller than the one observed in the blend. This result means that the observed 470-meV trap level is not formed by impurities from DCV5T-Me. This finding is particularly interesting, as it was previously observed that the DCV end groups can break during vacuum processing [43,44].

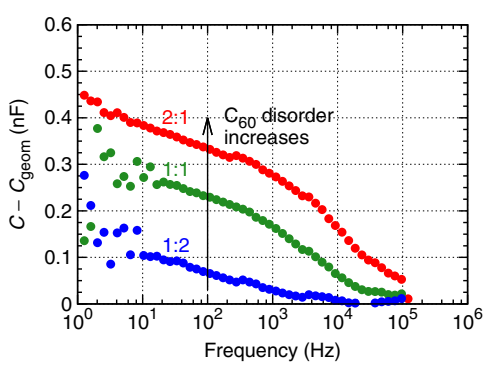

FIG. 7. *C-f* spectra for ITO/DCV5T-Me:C_{60}, 100 nm/Al with a varying mixture of DCV5T-Me:C_{60} ranging from 2:1 to 1:2.

TABLE III. Overview of the trap distributions measured in DCV5T-Me:C_{60}.

Mixing ratio[a]	Degradation	E_t (meV)	N_t (cm^{-3})	σ_t (meV)	ν_0 (s^{-1})
2:1	⋯	470	8.0×10^{14}	41	5.0×10^{11}
2:1	Air	365	3.0×10^{15}	35	2.8×10^{9}
2:1	O_2	368	6.8×10^{15}	27	1.5×10^{9}
1:1	⋯	484	5.0×10^{14}	41	3.0×10^{11}

[a]By volume.

C-f spectra for blends with varied mixing ratios are shown in Fig. 7. A decrease of the DCV5T-Me content in the blend leads to a decrease in trap capacitance, indicating a decrease of the amount of trap states. The DOS for the 1:1 blend (see the Supplemental Material [25]) has a Gaussian distribution with $E_t = 484$ meV, $N_t = 5 \times 10^{14}$ cm^{-3}, $\sigma_t = 41$ meV, and $\nu_0 = 3e11$ s^{-1}. The trap energy is similar to that determined for the 2:1 blend, but the density is lower (see Table III). For the 1:2 blend, the signal is too low to determine the DOS. Altogether, the change in trap capacitance is due to a change in N_t, not a change of the type of the defect. However, the trap signals cannot arise from intrinsic trap states from the donor phase, as we determine a very low trap contribution in DCV5T-Me–only devices, which is lower than that observed in 2:1 blend (see the Supplemental Material [25]). The trap states cannot be attributed to intrinsic defects in C_{60} either, as the amount of states goes down with larger C_{60} content. Moreover, IS measurements of ITO/C_{60}, 50 nm/BPhen, 8 nm/Al devices show only a shallow trap state with a depth of 100 meV ($\nu_0 = 2e5$ s^{-1}) in neat C_{60} (see the Supplemental Material [25]). Therefore, we relate the trap state with a depth of 470 meV to structural defects due to the intermixing of DCV5T-Me and C_{60}.

Even though a range of literature shows trap states in C_{60}, the measurements were done either in the doped systems [12] or in transistor geometry [45–47], introducing additional defects to C_{60}. Therefore, these data are not directly comparable to our measurements of neat C_{60}.

The intermixing of two materials changes their morphology from rather crystalline towards more nanocrystalline or even amorphous layers. When the ratio of C_{60} in the blend increases, the morphology of the C_{60} phase in the blend will approach the morphology of neat C_{60}, leading to a decreased number of structural defects. This behavior is demonstrated with x-ray diffraction measurements on layers of neat C_{60} and DCV5T-Me:C_{60}, respectively, showing the decrease of crystallinity of C_{60} in the blend [20]. The same trend is expected for DCV5T-Me. Hence, a variation in the mixing ratio leads to a higher crystallinity in one phase and a lower crystallinity in the other phase, which should have the opposite effect on the amount of trap states and *C-f* spectra. If the trap states came from the distortion of the crystallinity in the donor phase, they would

produce a maximal contribution to C-f signal in the 1:2 blend and a minimal one in the 2:1 blend, as discrepancy of donor morphology from neat DCV5T-Me increases with a lowered DCV5T-Me content. However, this is not the case (Fig. 7). Therefore, we conclude that there are no deep ($E_t < 200$ meV) structural defects in the donor phase that act as electron traps. For the C_{60} phase, the situation is the opposite. The distortion of C_{60} is maximal in the 2:1 blend and minimal in the 1:2 blend, which should increase the amount of trap states with a decreasing C_{60} content, as we observe.

We thus conclude that the observed trap states [Fig. 4(b)] are structural defects, coming from the distorted morphology of C_{60} near the interface between donor and acceptor, due to the mixing with DCV5T-Me.

VI. CONCLUSION

In this paper, we investigate the energetic distribution and the origin of trap states in blend layers of the high-efficiency donor material DCV5T-Me and C_{60} as the acceptor material and show that DCV5T-Me:C_{60} contains deep electron trap states with a Gaussian distribution with $E_t = 470$ meV, $N_t = 8 \times 10^{14}$ cm^{-3}, $\sigma_t = 41$ meV. These defects decrease the FF and the solar-cell performance and lead to trap-assisted recombination, which becomes dominant at light intensities below 0.01 sun. From air and oxygen degradation measurements, we find that these trap states cannot come from such degradation effects as the corresponding trap energies are more shallow (370 meV). We investigate blends with varied DCV5T-Me content, neat DCV5T-Me, and degraded blends with impedance spectroscopy measurements. We find the observed trap states to be structural defects in the C_{60} phase due to the distorted natural morphology induced by the mixing. Drift-diffusion simulations show that there is room for improving the FF when the trap densities are further reduced.

ACKNOWLEDGMENTS

The authors gratefully acknowledge their fruitful discussions with Janine Fischer and Paul Pahner, as well as useful comments on the manuscript from Hans Kleemann. We thank Selina Olthof for providing the UPS data and the Baeuerle group (University of Ulm) for originally developing the DCV5T-Me. Financial support came from the German Academic Exchange Service (DAAD, Forschungsstipendien für Doktoranden und Nachwuchswissenschaftler für mehr als 6 Monate, 57076385), Graduate Academy of Technical University of Dresden (DAAD-STIBET Completion Grant, PSP-Element:F-002401-536-601-3585101), Gesellschaft von Freunden und Foerderern der TU Dresden (DAAD scholarship STIBET III, Az.:147/2017, 147-2/2017), and the BMBF projects UNVEiL (13N13720) and InnoProfile (03IPT602X).

[1] Xiaozhou Che, Xin Xiao, Jeramy D. Zimmerman, Dejiu Fan, and Stephen R. Forrest, High-efficiency, vacuum-deposited, small-molecule organic tandem and triple-junction photovoltaic cells, Adv. Energy Mater. **4**, 1400568 (2014).

[2] Sunsun Li, Long Ye, Wenchao Zhao, Shaoqing Zhang, Subhrangsu Mukherjee, Harald Ade, and Jianhui Hou, Energy-level modulation of small-molecule electron acceptors to achieve over 12% efficiency in polymer solar cells, Adv. Mater. **28**, 9423 (2016).

[3] Wenchao Zhao, Deping Qian, Shaoqing Zhang, Sunsun Li, Olle Inganäs, Feng Gao, and Jianhui Hou, Fullerene-free polymer solar cells with over 11% efficiency and excellent thermal stability, Adv. Mater. **28**, 4734 (2016).

[4] Wenchao Zhao, Sunsun Li, Huifeng Yao, Shaoqing Zhang, Yun Zhang, Bei Yang, and Jianhui Hou, Molecular optimization enables over 13% efficiency in organic solar cells, J. Am. Chem. Soc. **139**, 7148 (2017).

[5] Abd Rashid bin Mohd Yusoff, Dongcheon Kim, Hyeong Pil Kim, Fabio Kurt Shneider, Wilson Jose da Silva, and Jin Jang, High efficiency solution processed polymer inverted triple-junction solar cell exhibiting conversion efficiency of 11.83%, Energy Environ. Sci. **8**, 303 (2015).

[6] Chun Chao Chen, Wei Hsuan Chang, Ken Yoshimura, Kenichiro Ohya, Jingbi You, Jing Gao, Zirou Hong, and Yang Yang, An efficient triple-junction polymer solar cell having a power conversion efficiency exceeding 11%, Adv. Mater. **26**, 5670 (2014).

[7] Huiqiong Zhou, Yuan Zhang, Cheng Kang Mai, Samuel D. Collins, Guillermo C. Bazan, Thuc Quyen Nguyen, and Alan J. Heeger, Polymer homo-tandem solar cells with best efficiency of 11.3%, Adv. Mater. **27**, 1767 (2015).

[8] John A. Carr and Sumit Chaudhary, The identification, characterization and mitigation of defect states in organic photovoltaic devices: A review and outlook, Energy Environ. Sci. **6**, 3414 (2013).

[9] M. M. Mandoc, F. B. Kooistra, J. C. Hummelen, B. De Boer, and P. W. M. Blom, Effect of traps on the performance of bulk heterojunction organic solar cells, Appl. Phys. Lett. **91**, 263505 (2007).

[10] Loren Kaake, Xuan-Dung Dang, Wei Lin Leong, Yuan Zhang, Alan Heeger, and Thuc-Quyen Nguyen, Effects of impurities on operational mechanism of organic bulk heterojunction solar cells, Adv. Mater. **25**, 1706 (2013).

[11] C. Li, L. Duan, H. Li, and Y. Qiu, Universal trap effect in carrier transport of disordered organic semiconductors: Transition from shallow trapping to deep, J. Phys. Chem. C **118**, 10651 (2014).

[12] Selina Olthof, Shafigh Mehraeen, Swagat K. Mohapatra, Stephen Barlow, Veaceslav Coropceanu, Jean Luc Brédas, Seth R. Marder, and Antoine Kahn, Ultralow Doping in Organic Semiconductors: Evidence of Trap Filling, Phys. Rev. Lett. **109**, 176601 (2012).

[13] Tanvir Muntasir and Sumit Chaudhary, Defects in solution-processed dithienylsilole-based small-molecule photovoltaic thin-films, J. Appl. Phys. **119**, 025501 (2016).

[14] Janine Fischer, Debdutta Ray, Hans Kleemann, Paul Pahner, Martin Schwarze, Christian Koerner, Koen Vandewal, and Karl Leo, Density of states determination in organic

donor-acceptor blend layers enabled by molecular doping, J. Appl. Phys. **117**, 245501 (2015).

[15] Tanvir Muntasir and Sumit Chaudhary, Understanding defect distributions in polythiophenes via comparison of regioregular and regiorandom species, J. Appl. Phys. **118**, 205504 (2015).

[16] Donato Spoltore, Wibren D. Oosterbaan, Samira Khelifi, John N. Clifford, Aurelien Viterisi, Emilio Palomares, Marc Burgelman, Laurence Lutsen, Dirk Vanderzande, and Jean Manca, Effect of polymer crystallinity in P3HT:PCBM solar cells on band gap trap states and apparent recombination order, Adv. Energy Mater. **3**, 466 (2013).

[17] Samira Khelifi, Koen Decock, Johan Lauwaert, Henk Vrielinck, Donato Spoltore, Fortunato Piersimoni, Jean Manca, Abderrahmane Belghachi, and Marc Burgelman, Investigation of defects by admittance spectroscopy measurements in poly (3-hexylthiophene):(6,6)-phenyl C61-butyric acid methyl ester organic solar cells degraded under air exposure, J. Appl. Phys. **110**, 094509 (2011).

[18] V. Dyakonov, D. Godovsky, J. Meyer, J. Parisi, C. J. Brabec, N. S. Sariciftci, and J. C. Hummelen, Electrical admittance studies of polymer photovoltaic cells, Synth. Met. **124**, 103 (2001).

[19] Rico Meerheim, Christian Körner, and Karl Leo, Highly efficient organic multi-junction solar cells with a thiophene based donor material, Appl. Phys. Lett. **105**, 063306 (2014).

[20] Roland Fitzner, Elena Mena-Osteritz, Amaresh Mishra, Gisela Schulz, Egon Reinold, Matthias Weil, Christian Körner, Hannah Ziehlke, Chris Elschner, Karl Leo, Moritz Riede, Martin Pfeiffer, Christian Uhrich, and Peter Bäuerle, Correlation of π-conjugated oligomer structure with film morphology and organic solar cell performance, J. Am. Chem. Soc. **134**, 11064 (2012).

[21] Christian Körner, Ph.D. thesis, Technische Universität Dresden, 2012.

[22] A. Baumann, J. Lorrmann, D. Rauh, C. Deibel, and V. Dyakonov, A new approach for probing the mobility and lifetime of photogenerated charge carriers in organic solar cells under real operating conditions, Adv. Mater. **24**, 4381 (2012).

[23] J. Lorrmann, B. H. Badada, O. Inganäs, V. Dyakonov, and C. Deibel, Charge carrier extraction by linearly increasing voltage: Analytic framework and ambipolar transients, J. Appl. Phys. **108**, 113705 (2010).

[24] Kristofer Tvingstedt and Carsten Deibel, Temperature dependence of ideality factors in organic solar cells and the relation to radiative efficiency, Adv. Energy Mater. **6**, 1502230 (2016).

[25] See Supplemental Material at http://link.aps.org/supplemental/10.1103/PhysRevApplied.9.024039 for *C-f* spectra for an ITO/DCV5*T*-Me:C_{60}/Al device stored in different atmospheres, *C-f* spectra for ITO/DCV5*T*-Me:C_{60}/Al devices with varied blend thicknesses, absolute values of the fingerprints for the simulated *I-V* curves, *C-f* spectra for neat DCV5T-Me, and trap DOSs in a 1:1 blend and in neat C_{60}.

[26] Carl Poelking, Max Tietze, Chris Elschner, Selina Olthof, Dirk Hertel, Klaus Meerholz, Karl Leo, and Denis Andrienko, Impact of mesoscale order on open-circuit voltage in organic solar cells, Nat. Mater. **14**, 434 (2015).

[27] Hiroyuki Yoshida, New Experimental Method to Precisely Examine the LUMO Levels of Organic Semiconductors and Application to the Fullerene Derivatives, in *Symposium E/H—Photovoltaic Technologies, Devices and Systems Based on Inorganic Materials, Small Organic Molecules and Hybrids*, MRS Symposia Proceedings No. 1493 (Materials Research Society, Pittsburgh, 2013), p. 295.

[28] Moritz Hein, diploma thesis, Technische Universität Dresden, 2011 (mobility was measured in an OFET geometry).

[29] A. V. Nenashev, J. O. Oelerich, and S. D. Baranovskii, Theoretical tools for the description of charge transport in disordered organic semiconductors, J. Phys. Condens. Matter **27**, 093201 (2015).

[30] V. I. Arkhipov, E. V. Emelianova, and G. J. Adriaenssens, Effective transport energy versus the energy of most probable jumps in disordered hopping systems, Phys. Rev. B **64**, 125125 (2001).

[31] Juan Bisquert, Beyond the quasistatic approximation: Impedance and capacitance of an exponential distribution of traps, Phys. Rev. B **77**, 235203 (2008).

[32] T. Walter, R. Herberholz, C. Müller, and H. W. Schock, Determination of defect distributions from admittance measurements and application to $Cu(In,Ga)Se_2$ based heterojunctions, J. Appl. Phys. **80**, 4411 (1996).

[33] Wolfgang Tress, Karl Leo, and Moritz Riede, Dominating recombination mechanisms in organic solar cells based on ZnPc and C60, Appl. Phys. Lett. **102**, 163901 (2013).

[34] Liang Xu, Jian Wang, and Julia W. P. Hsu, Transport Effects on Capacitance-Frequency Analysis for Defect Characterization in Organic Photovoltaic Devices, Phys. Rev. Applied **6**, 064020 (2016).

[35] J. David Cohen and David V. Lang, Calculation of the dynamic response of Schottky barriers with a continuous distribution of gap states, Phys. Rev. B **25**, 5321 (1982).

[36] Debdutta Ray and K. L. Narasimhan, Measurement of deep states in hole doped organic semiconductors, J. Appl. Phys. **103**, 093711 (2008).

[37] L. Burtone, D. Ray, K. Leo, and M. Riede, Impedance model of trap states for characterization of organic semiconductor devices, J. Appl. Phys. **111**, 064503 (2012).

[38] X. M. Ding, L. M. Hung, L. F. Cheng, Z. B. Deng, X. Y. Hou, C. S. Lee, and S. T. Lee, Modification of the hole injection barrier in organic light-emitting devices studied by ultraviolet photoelectron spectroscopy, Appl. Phys. Lett. **76**, 2704 (2000).

[39] Y. Park, V. Choong, Y. Gao, B. R. Hsieh, and C. W. Tang, Work function of indium tin oxide transparent conductor measured by photoelectron spectroscopy, Appl. Phys. Lett. **68**, 2699 (1996).

[40] Measured with UPS in-house.

[41] Measured for BPAPF:NDP9 10 wt % with UPS by Selina Olthof.

[42] Paul Pahner, Ph.D. thesis, Technische Universität Dresden, 2016.

[43] Hannah Ziehlke, Ph.D. thesis, Technische Universität Dresden, 2011.

[44] *Elementary Processes in Organic Photovoltaics*, 1st ed., edited by Karl Leo (Springer International Publishing, Cham, Switzerland, 2017), p. 55.

[45] Toshinori Matsushima, Masayuki Yahiro, and Chihaya Adachi, Estimation of electron traps in carbon-60 field-effect transistors by a thermally stimulated current technique, Appl. Phys. Lett. **91**, 103505 (2007).

[46] Naoko Kawasaki, Takayuki Nagano, Yoshihiro Kubozono, Yuuki Sako, Yu Morimoto, Yutaka Takaguchi, Akihiko Fujiwara, Chih-Chien Chu, and Toyoko Imae, Transport properties of field-effect transistor with Langmuir-Blodgett films of dendrimer and estimation of impurity levels, Appl. Phys. Lett. **91**, 243515 (2007).

[47] Wolfgang L. Kalb, Simon Haas, Cornelius Krellner, Thomas Mathis, and Bertram Batlogg, Trap density of states in small-molecule organic semiconductors: A quantitative comparison of thin-film transistors with single crystals, Phys. Rev. B **81**, 155315 (2010).